AIAA AVIATION Forum
5-9 June 2017, Denver, Colorado
47th AIAA Fluid Dynamics Conference

10.2514/6.2017-4419

Numerical Investigation of the Interaction of Active Flow Control and Klebanoff Modes

Shirzad Hosseinverdi[1], Hermann F. Fasel[2]
Department of Aerospace and Mechanical Engineering
The University of Arizona, Tucson, AZ 85721

Highly resolved direct numerical simulations (DNS) are employed to investigate active flow control of laminar boundary-layer separation by means of two-dimensional harmonic blowing and suction through a narrow spanwise slot. The uncontrolled flow configurations are represented by laminar separation bubbles (LSBs) generated on a flat plate by an adverse pressure gradient according to earlier wind-tunnel experiments by Gaster.[1] Active flow control is shown to significantly reduce the separation region. In agreement with our previous research the effectiveness of the flow control can be explained by the fact that the primary shear-layer instability is exploited. Furthermore, it is demonstrated that two-dimensional periodic forcing with a properly chosen frequency and amplitude can suppress the growth of three-dimensional disturbances and thus delays transition to turbulence, and even can relaminarize the flow. To investigate the effects of a realistic flow environment, very low-amplitude isotropic free-stream turbulence (FST) fluctuations are introduced at the inflow boundary. With FST the effectiveness of the flow control is not diminished and the extent of the separated flow region is reduced by the same amount as for the zero FST case. However, a striking difference is that in the presence of even very low FST, the flow transitions shortly downstream of the reattachment location of the bubble. It appears that this different behavior for even very small levels of FST is caused by an interaction between the high-amplitude 2D wave introduced by the forcing and the 3D Klebanoff modes caused by the FST. The streamwise streaks due to the Klebanoff modes cause a spanwise-periodic modulation of the primary 2D wave. The disturbances associated with this modulation exhibit strong growth and initiate transition via a continuous formation of Λ-vortices. Therefore, the relaminarization of the flow does not occur in a realistic environment, even for very low FST levels.

I. Introduction

WHEN subjected to a strong enough adverse pressure gradient, a laminar boundary-layer will detach from the wall, and for sufficiently large Reynolds numbers, the separated flow will transition in the separated region thus creating a so-called laminar separation bubble. The size and nature of the separated region itself affect the circulation (e.g., for an airfoil) and, thereby, separation itself. In general, flow separation has to be avoided because it negatively affects airplane performance. Large separation bubbles can drastically reduce the aerodynamic efficiency by reducing the usable lift and increasing drag. Another aspect is the increase in flow unsteadiness and noise caused by flow separation.

For flight vehicles, successful active flow control (AFC) of boundary-layer separation for lifting surfaces could lead to significant performance gains. This is especially true for Unmanned Aerial Vehicles (UAVs), which have become increasingly important for military operations. Due to the usually small wing dimensions and low air-speeds, UAVs often operate within a Reynolds-number flight regime, for which a strong interaction exists between separation and transition. An improved understanding of the relevant physical mechanisms, especially in the presence of free-stream turbulence (FST), is required for effective flow control.

Previous studies have shown that flow control that exploits the shear-layer instability is both effective and efficient for controlling laminar separation at low-Reynolds numbers [2-6]. The primary convective instability strongly amplifies the disturbance waves (within the Kelvin-Helmholtz frequency range of the separated shear layer)

[1] PhD candidate, AIAA member.
[2] Professor, AIAA Associate Fellow.

introduced upstream of the separation location until they saturate at a finite nonlinear amplitude, leading to the commonly observed periodic shedding of spanwise coherent vortical structures. The presence of the large-amplitude waves (or vortices) facilitates an exchange of momentum, which limits the extent of the separation region.

In addition to reducing the extent of the separated flow region, Embacher & Fasel[2] showed that high-amplitude two-dimensional (2D) disturbance waves with a properly chosen frequency and amplitude can suppress the secondary absolute instability and thus delay transition and even relaminarize the flow downstream of reattachment. In these high-order accurate, numerical simulations the effects of realistic operation conditions, such as free-stream turbulence, noise and vibrations were neglected. Therefore, the question arises whether the observed transition delay and relaminarization of the flow is still possible in a "real" environment as encountered in free flight or wind/water-tunnel experiments.

For airplane applications, it is reasonable to assume that surface roughness and free-stream turbulence can provide the disturbances that lead to laminar-turbulent transition. Both have to be considered when investigating separation and separation control. The present work is aimed at investigating whether FST affects the stunning effectiveness of the 2D harmonic excitation for transition delay and relaminarization. Towards this end, very low-amplitude isotropic FST velocity and vorticity fluctuations are introduced at the inflow boundary of the computational domain.

For the present investigations, laminar separation bubbles on a flat plate caused by a favorable-to-adverse streamwise pressure gradient are considered. The simulations discussed here are based on the conditions of the wind tunnel experiments by Gaster[1], specifically series I case IV ("short" LSB), and case VI ("long" LSB). The simulation set-up and key aspects of the computational grid are discussed in Section II. The governing equations, the numerical method, the procedure for generating the FST, and the flow control details are provided in Section III. Characteristic features of the uncontrolled flow for both zero and non-zero FST conditions are discussed in section IV. A detailed discussion of the results for the controlled LSBs is provided in section V. Finally, a summary of the results is provided.

II. Simulation Set-Up

The set-up of the numerical simulations was guided by the experimental investigations of laminar separation bubbles by Gaster.[1] In the experiments, laminar separation on a flat plate is induced through the close proximity of an auxiliary wing that is mounted upside down in the wind tunnel. Gaster[1] also provided measurements where the boundary layer was tripped to turbulence and therefore did not separate in order to get an approximate 'inviscid' solution for the streamwise pressure gradient. The wall-normal velocity distributions at the upper domain boundary of the computational domain for the DNS were specified to reproduce the 'inviscid' wall pressure distributions reported by the Gaster's series I experiments, (see Fig. 2).

Depending on the governing parameters, such as Reynolds number and pressure distribution, LSBs can be classified as either "short" or "long". There are several parameters proposed by researchers to determine whether a bubble is "short" or "long" (see for example, Gaster[1], Owen & Klanfer[7] and Diwan et al.[8]). However, it seems more intuitive to classify a bubble as either "short" or "long" based on their effect on the pressure distribution. Towards this end, the effect of a separation bubble on the pressure distribution is local and limited in the case of a "short" bubble while a "long" bubble has a strong upstream and downstream impact on the inviscid pressure field.

By varying the tunnel speed, Gaster[1] generated a series of "short" and "long" separation bubbles. The present investigation focuses on both a "long" bubble (case VI) and a "short" bubble (case IV). The velocity scales are chosen according to the tunnel speed in the experiments, $U_\infty^* = 6.64[m/s]$ for case VI and $U_\infty^* = 12.192[m/s]$ for case IV. The reference length scale is $L_\infty^* = 1[in] = 0.0254[m]$. This length scale is chosen because the experimental data were reported in inches. The chord length of the wing section in the experiments is $C^* = 5.5[in]$ and the global Reynolds number based on C^* and U_∞^* are $Re_{C^*} = 61{,}840$ and $Re_{C^*} = 113{,}550$ for cases VI and IV, respectively. The asterisk is used to denote dimensional quantities.

For our simulations, we employ our high-order-accurate, spatial DNS code for a model geometry (separation is generated on a flat plate as in the experiments). This model geometry is defined such that it exhibits a flow with similar physical properties as the flow over an airfoil but at reduced geometric complexity. This approach will enable higher grid resolution and the use of a considerably more efficient incompressible DNS code, which will allow capturing of the relevant physics with greater confidence.

The computational domain is depicted in Fig. 2. The integration domain does not include the leading edge. The streamwise coordinate is x, the spanwise coordinate is z, and the wall-normal coordinate is y. The domain extent and computational grid parameters are summarized in Tab. 1 for each case. The grid spacing is uniform in the streamwise direction. An exponential grid point distribution was employed in the wall-normal direction to improve the near-wall resolution. Length scales were made dimensionless with a reference length of L_∞^*, and velocities were made dimensionless with a reference velocity U_∞^*. A Blasius velocity profile is prescribed at the inflow. The Reynolds

number based on the inflow displacement thickness and the free-stream streamwise velocity at the inflow boundary is $Re_{\delta_1} = 407.8$ and $Re_{\delta_1} = 552.6$ for case VI and case IV, respectively.

In Gaster's experiments at the separation location, the boundary-layer edge velocity and Reynolds number based on the momentum thickness were $u_{e,S} = 1.3$ and $Re_{\theta,S} = 218$ for case L ("long" bubble) and $u_{e,S} = 1.355$ and $Re_{\theta,S} = 298$ for case S ("short" bubble). In the DNS, these values are $u_{e,S} = 1.32$ and $Re_{\theta,S} = 189$ for case L and $u_{e,S} = 1.37$ and $Re_{\theta,S} = 252$ for case S, which compare favorably to the values measured in the experiments.

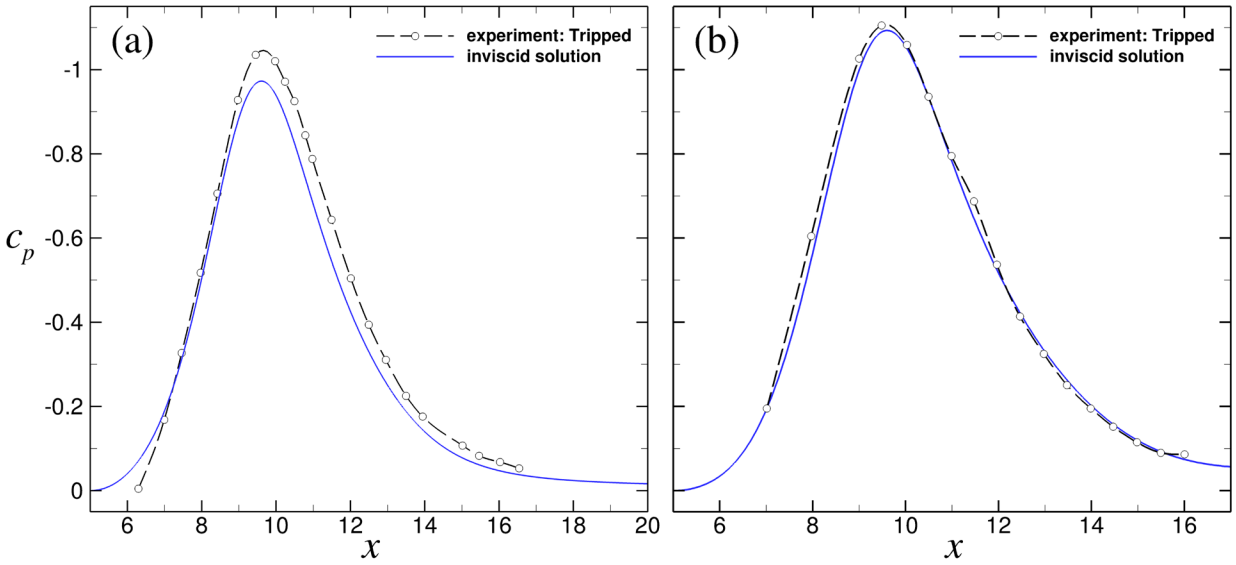

Figure 1. Wall-pressure coefficient: (—) inviscid solution; (○) experiment tripped to turbulence for Series I experiments by Gaster[1]: (a) Case VI, (b) case IV.

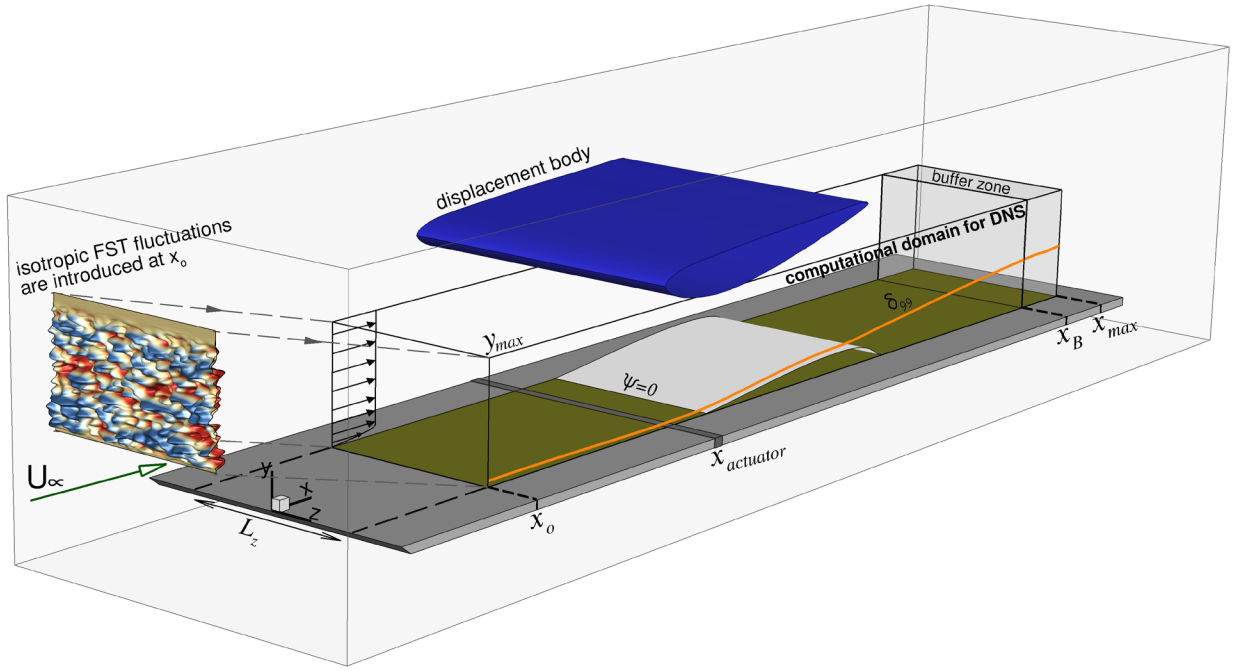

Figure 2. Schematic of the computational setup. Isotropic FST fluctuations are seeded at the inflow boundary. Flow control is applied at $x_{actuator}$.

case	$x_0 \times x_{max} \times y_{max} \times L_z$	$n_x \times n_x \times n_x$	$\Delta x^+ \times \Delta y^+_{wall} \times \Delta z^+$
L	5×21.2×2×2	1801×256×200	5.54×0.95×6.16
S	5×17.95×2×1	3501×340×270	4.35×0.43×4.36

Table 1. Parameters for the computational domain as shown in Fig. 2. Case *L* corresponds to Gaster case VI, ("long" bubble) and case *S* to Gaster case IV ("short" bubble). The grid resolution in wall units are based on a maximum skin-friction coefficient in the developing turbulent boundary layer.

III. Numerical Methodology

Direct Numerical Simulation (DNS) of transition requires numerical methods with low numerical dispersion and dissipation. Therefore, a three-dimensional incompressible Navier-Stokes code, using a combination of high-order accurate finite-difference approximations and a pseudo-spectral method, was employed. This code was developed in our CFD Laboratory and validated for numerous cases of boundary-layer transition (Meitz & Fasel[9]), laminar separation bubbles in two and three-dimensional boundary-layers (Balzer & Fasel[10], Hosseinverdi et al.[11], Hosseinverdi & Fasel[12]), and separation control (Hosseinverdi & Fasel[13]; Postl et al.[14]). The following section provides a summary of the numerical method and the computational approach.

A. Governing Equations

The governing equations are the incompressible, unsteady Navier-Stokes equations in vorticity velocity formulation. The transport equation for the vorticity vector $\boldsymbol{\omega}$ is

$$\frac{\partial \boldsymbol{\omega}}{\partial t} = \boldsymbol{\nabla} \times (\boldsymbol{u} \times \boldsymbol{\omega}) + \frac{1}{Re} \boldsymbol{\nabla}^2 \boldsymbol{\omega} \,. \tag{1}$$

Here the vorticity is defined as the negative curl of the velocity $\boldsymbol{\omega} = -\boldsymbol{\nabla} \times \boldsymbol{u}$. Equation (1) consists of three transport equations for the vorticity components in the streamwise (x), wall-normal (y) and spanwise (z) directions, respectively. The global Reynolds number in equation 1 is defined as $Re = U^*_\infty L^*_\infty / \nu^*$, where ν^* is the kinematic viscosity. Using the fact that the both vorticity and velocity vector fields are solenoidal, one can obtain a vector Poisson equation for the velocity field,

$$\nabla^2 \boldsymbol{u} = \boldsymbol{\nabla} \times \boldsymbol{\omega} \tag{2}$$

B. Numerical Method

The governing equations are integrated in time using an explicit fourth-order-accurate Runge–Kutta scheme. All derivatives in streamwise and wall-normal directions are approximated with fourth-order compact differences. No explicit filtering is used in present investigations. Instead stability is enhanced by appropriate treatment of the first derivative of the nonlinear terms, which are discretized using fourth-order accurate (split) compact differences in x-direction. At consecutive sub-steps of the four-stage Runge–Kutta scheme, the numerical scheme alternates between upwind-biased differences and downwind-biased differences. In the wall-normal direction, an exponential grid stretching is used in order to cluster grid points near the wall. Note that the finite-difference approximations for the derivatives with respect to y are constructed for a non-equidistant grid instead of using a coordinate transformation. While this approach is tedious, it can yield higher accuracy than the traditional method of grid stretching by using a coordinate transformation.

The flow field is assumed to be periodic in the spanwise direction. Therefore, the flow field is expanded in Fourier cosine and sine series. Each variable is represented by a total of 2K+1 Fourier modes: the 2D spanwise average (zeroth Fourier mode), K symmetric Fourier cosine as well as K antisymmetric Fourier sine modes. To avoid aliasing errors, the nonlinear terms in physical space are computed on K ≈ 3K spanwise collocation points.

Fast Fourier Transforms (FFTs) are employed to convert each variable from spectral space to physical space and vice versa. The nonlinear terms are computed in physical space, while differentiation, integration, and imposition of the boundary conditions take place in spectral space. For the calculation of the nonlinear terms, the flow field is transformed from spectral to physical space (and back) before each Runge-Kutta sub-step, which requires redistributing of the entire three-dimensional arrays among the processors. This extensive inter-processor communication is realized using the message passing interface (MPI).

The velocity Poisson equation (2) is solved by a direct method using fourth-order standard compact differences in wall-normal direction and Fourier sine transforms in streamwise direction.

C. Boundary Conditions

The flow enters the computational domain at the inflow boundary located at x_0, and leaves it through the outflow boundary at x_{max}. In the spanwise direction, the flow is assumed to be periodic with the fundamental wavelength $\lambda_z = L_z$, where L_z is the domain width in spanwise direction.

At the inflow boundary at $x = x_0$ all velocity and vorticity components are specified. In particular, the velocity and vorticity components of a two-dimensional (2-D) steady-state basic flow obtained from the Blasius equations, superimposed with velocity and vorticity fluctuations from the FST model, are prescribed as Dirichlet conditions. In addition, for maintaining the fourth-order accuracy of the code near the inflow boundary, the streamwise derivatives are prescribed as well.

At the outflow boundary, $x = x_{max}$, all second derivatives in streamwise direction are set to zero. In addition, a buffer domain in region $x_B < x < x_{max}$ as proposed by Meitz & Fasel[9], is employed in order to smoothly dampen out the fluctuations generated inside the domain. Note that near the outflow boundary, the boundary layer is turbulent and large errors would occur if a laminar boundary–layer solution would be enforced at the outflow boundary. Therefore, within the buffer region, the solution was ramped down to turbulent mean flow profiles, which were obtained from precursor simulations with a longer integration domain.

The no-slip and no-penetration conditions are enforced on the surface of the flat plate. In addition, the wall-normal derivative of the v-velocity is set to zero to ensure conservation of mass. At the free-stream boundary $y = y_{max}$ it is assumed that the flow is irrotational, thus all vorticity components and their derivatives are set to zero. A wall-normal velocity distribution is applied at the upper boundary for generating the favorable to adverse pressure gradients that induces laminar separation on the flat plate. The v-velocity distribution is chosen such that the resulting downstream pressure gradient closely matches that of the wind-tunnel experiments by Gaster.[1]

D. Free-Stream Turbulence Generation

The LSBs investigated here are subjected to the FST, which was modeled by introducing a set of velocity and vorticity disturbances at the inflow boundary of the domain. The methodology adopted for generating realistic free-stream turbulence velocity fluctuations at the inflow boundary is similar to that proposed by Jacobs & Durbin.[15] The method is based on a Fourier expansion of the disturbance velocity with random amplitudes:

$$\boldsymbol{u}'(\boldsymbol{x},t) = \sum_{k} \hat{\boldsymbol{u}}(\boldsymbol{k},t) e^{i\boldsymbol{k}\cdot\boldsymbol{x}}\,, \tag{3}$$

where the wavenumber vector is $\boldsymbol{k} = \left[k_x, k_y, k_z\right]^T$ with $k = |\boldsymbol{k}|$. Here k_x, k_y and k_z are the streamwise, wall-normal and spanwise wavenumbers, respectively. In the same manner, the inflow disturbance vorticity field is calculated from the disturbance velocity field as $\boldsymbol{\omega}' = -\nabla\times\boldsymbol{u}'$.

The objective is to specify the Fourier coefficients of a disturbance velocity field such that the inlet disturbance flow field satisfies continuity and generates isotropic turbulence in the free-stream and models a specified energy spectrum. By invoking Taylor's hypothesis and ignoring the streamwise decay, $k_x x$ can be replaced by a -ωt, where ω is the angular disturbance frequency. The implementation of the spanwise Fourier modes, $e^{ik_z z}$, is straightforward since the numerical model assumes periodicity of the flow field in z-direction. However, in the presence of an inhomogeneous direction y, specific basis functions are needed to account for the presence of the wall. Instead of Fourier modes $\left(\exp(ik_y y)\right)$ in the expansion of the disturbance quantities, Jacobs & Durbine[15] and Brandt et.al.[16] suggested to use eigenmodes from the continuous spectrum of the Orr-Sommerfeld and Squire operators since they are sinusoidal in the free-stream, but naturally decay inside the boundary layer (see Grosch & Salwen[17]). Therefore Eq. 3 can be reformulated as

$$\boldsymbol{u}'(x_0,y,z,t) = \sum_{\omega}\sum_{k_z}\sum_{k_y} A\,(|k|)\Phi\left(\omega,k_y,k_z\right) e^{ik_z z} e^{-i\omega t}\,. \tag{4}$$

Here, the coefficients $A(|k|)$ determine the contribution of the eigenfunctions to the total turbulent kinetic energy and Φ is a normalized superposition of Orr–Sommerfeld, Φ_{OS}, and Squire, Φ_{SQ}, continuous eigenfunctions. The velocity fluctuations at the inflow model the specified energy spectrum. Various analytic forms for energy spectrum exist. For

most of the simulations presented in this work, the von Karman energy spectrum is employed for distributing the turbulent kinetic energy among the various modes

$$E(k) = Tu_0^2 L_{11} \frac{1.196(kL_{11})^4}{0.558[1 + (kL_{11})^2]^{17/6}}. \tag{5}$$

The turbulent integral length scale, L_{11}, determines the wavenumber associated with the maximum in the $E(k)$ distribution. For large scales (small k) the spectrum is asymptotically proportional to k^4. For small scales (large k) the spectrum matches Kolmogorov's $k^{-5/3}$law.

In order to obtain isotropic turbulence, several wavenumbers k have to be selected in the domain $k_{min} < k < k_{max}$, where the limiting wavenumbers are determined by the chosen numerical resolution. For the present investigations, the wavenumber space (k) was divided into 40 equidistant concentric shells over which energy was distributed discretely using a limited number, N_p, of disturbance modes. Modes on a given shell have an identical wave number magnitude, $|k| = \sqrt{\omega^2 + k_y^2 + k_z^2}$. The coefficient of each terms in equation (2.4) is given by $A(|k|) = \sqrt{2E(k)\Delta k/N_p}$, where Δk is difference in wavenumber between two shells. Finally, upon choosing the parameters L_{11} and the FST intensity Tu_0, the inflow velocity- and vorticity disturbance fields can be entirely determined. A detailed description of the implementation and validation results are provided in Balzer & Fasel[10] and Hosseinverdi et al.[11]

E. Flow Control: Harmonic Blowing and Suction Through 2D Slot

In the present simulation, high amplitude, two-dimensional disturbance waves are generated upstream of the separation location by specifying a wall-normal velocity component across a narrow blowing and suction slot at the wall. The forcing function for the harmonic blowing and suction (HBS) simulations has the form

$$v_f(x,t) = A \cdot F(x) \cdot \cos(\beta_f t + \theta_f), \tag{6}$$

where A is the maximum forcing amplitude and β_f & θ_f represent the angular forcing frequency and phase shift, respectively. The shape function, $F(x)$, is a polynomial which is zero outside the suction/blowing slot such that smooth derivatives near boundaries of the suction/blowing slot are obtained. Furthermore, this shape function guarantees zero net volume flow through the disturbance slot at any time instant:

$$F(x) = \frac{1}{48}\begin{cases} +729\psi^5 - 1701\psi^4 + 972\psi^3, & \psi = \dfrac{x - x_s}{x_f - x_s}; \quad x_s \le x \le x_f \\ -729\psi^5 + 1701\psi^4 - 972\psi^3, & \psi = \dfrac{x_e - x}{x_e - x_f}; \quad x_f \le x \le x_e \end{cases}, \tag{7}$$

The downstream locations x_s, x_e and x_f correspond the beginning, the end, and the center of the slot, respectively. The shape function for the spanwise slot actuation is plotted in Fig. 3.

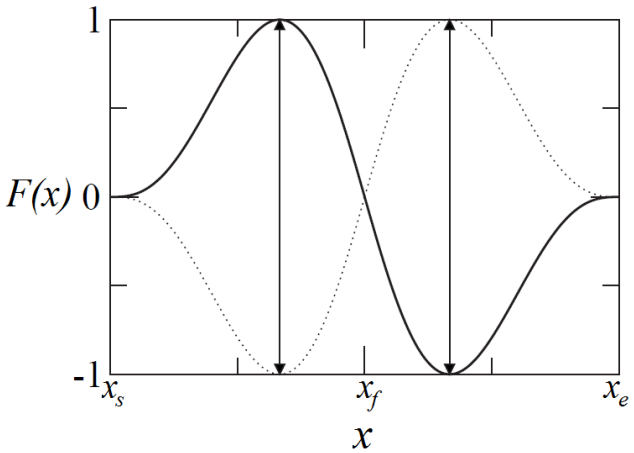

Figure 3. Wall-normal velocity distribution, *F*(*x*), for 2D harmonic blowing and suction slot.

IV. Characteristic Features of Uncontrolled Flow

In this section results obtained from 3D DNS of the uncontrolled flow for the two cases (S & L) are discussed in order to understand the relevant length scales and characteristic frequencies of the LSBs in the presence of FST and zero FST. For the FST simulations, a full spectrum of isotropic FST with an intensity of $Tu_0 = 0.005\%$ is introduced at the inflow boundary of the computational domain.

The free-stream vortical disturbances generated by the free-stream turbulence model are illustrated in Fig. 4. Because the vorticity associated with the turbulent velocity fluctuations in the free-stream is much smaller than the vorticity associated with the near wall structures, a logarithmic scale was employed for plotting the spanwise vorticity in the free-stream (averaged in the spanwise direction) in Fig. 4. For the zero FST environment, the free-stream is undisturbed (top plots). For the zero FST case, the boundary layer separates laminar and then undergoes transition to turbulence and reattaches. The transition onset shifts upstream with the inclusion of FST. It has been shown (e.g., Liu *et al*.[18]) that laminar boundary layers act as a low-pass filter, which means that low frequency vortical fluctuations can penetrate the laminar boundary layer and promote transition.

To gain insight into the transient 'roll-up' of vorticity from the separated shear layer, the temporal variation of the spanwise vorticity (averaged in spanwise direction) was analyzed for one full period of the dominant shedding frequency for case S in the absence of FST and is plotted in Fig. 5. In each image, the mean dividing streamlines are indicated by the solid lines while the dashed lines correspond to the mean displacement thickness. The oblique line identifies the instantaneous location of one of the coherent structures generated in the transition process for the five time instances. For a laminar separation bubble, because the velocity profiles in the separated region exhibit an inflection point, the separated shear-layer is highly unstable w.r.t. 2D disturbances, which therefore are strongly amplified. The resulting spanwise structures ("rollers") facilitate a transfer of high momentum fluid from the free-stream towards the wall and of low momentum fluid away from the wall, and thus promote mixing and ultimately reattachment. These spanwise vortical structures can persist even in the turbulent flow region downstream of the reattachment location (coherent structures). Examination of the transient roll-up of vorticity in the separated shear layer suggests that the roll-up takes place in three steps: (i) Onset of the roll-up upstream of the maximum bubble height, (ii) along the mean dividing streamline, the developed vortex ("spanwise roller") grows in intensity due to the Kelvin-Helmholtz instability as it is convected downstream, and (iii) it is shed at the location of the maximum bubble height. Also, small vortical structures are present near the wall, which are also contributing to the exchange of momentum.

To detect the dominant frequencies in the separation bubble, the time signal of the spanwise-averaged wall-normal disturbance velocity component, $v' = v - \bar{v}$, is monitored along the local displacement thickness, which is very close to the inflection point. Figs. 6 and 7 show the contours of v' in an x-t-diagram for cases L and S for zero FST and $Tu = 0.005\%$, respectively. A strong variation of the velocity signal with a distinct timescale (strong temporal periodicity) can be observed for all cases. The onset of temporal periodicity moves upstream with the presence of FST. The unsteadiness is directly related to the vortex shedding of the separation bubble and can typically be associated with the inviscid shear layer instability. A Fourier analysis of the signals is performed in order to obtain the frequency spectrum associated with these velocity signals. Results of the spectral analyses are presented in Figs. 6 and 7. From the spectral analysis, the following dominant frequencies are obtained:

- case L: $f^* = 234\ (hz)$ for $Tu = 0$ and $f^* = 276\ (hz)$ for $Tu = 0.005\%$.
- case S: $f^* = 633\ (hz)$ for $Tu = 0$ and $f^* = 733\ (hz)$ for $Tu = 0.005\%$.

The non-dimensional frequencies based on the free-stream velocity and the mean separation length are

- case L: $F^+ = 4.58$ for $Tu = 0$ and $F^+ = 4.46$ for $Tu = 0.005\%$.
- case S: $F^+ = 4.18$ for $Tu = 0$ and $F^+ = 4.54$ for $Tu = 0.005\%$.

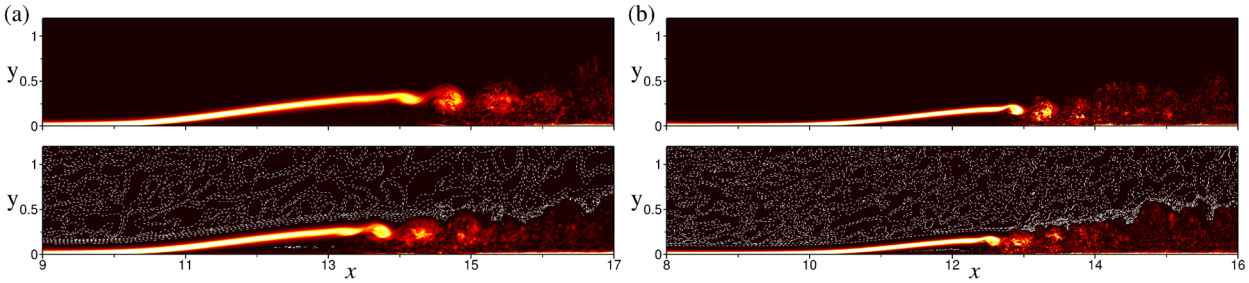

Figure 4. Instantaneous contours of spanwise vorticity, ω_z, for zero FST (top) and FST of $Tu = 0.005\%$ (bottom). Dashed contour lines correspond to $ln|\omega_z|$. (a) case L; (b) case S.

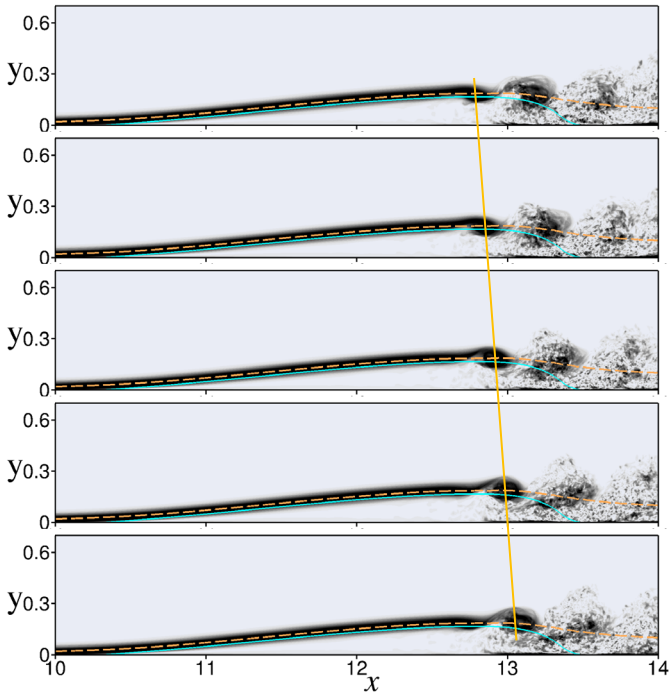

Figure 5. Instantaneous contours of spanwise vorticity, ω_z (averaged in spanwise direction) at five time instances for disturbance-free simulation, case *S*. Time instances are separated by one fifth the vortex-shedding period. The solid lines are the mean dividing stream line and dashed lines represent the mean displacement thickness.

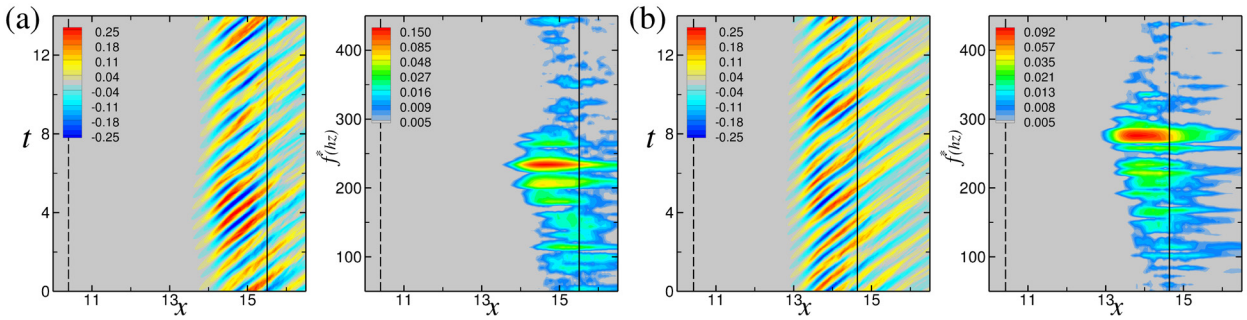

Figure 6. Contours of spanwise-averaged wall-normal disturbance velocity in t/x diagram extracted along the mean displacement thickness (left) and the respective Fourier spectra (right) for case *L*. (a) zero FST; (b) $Tu = 0.005\%$. The dashed and solid lines correspond to the mean separation and reattachment locations, respectively.

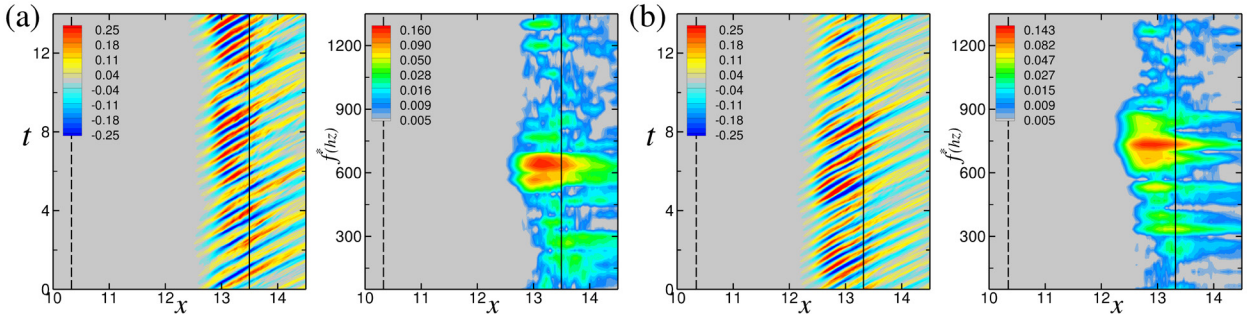

Figure 7. Contours of spanwise-averaged wall-normal disturbance velocity in t/x diagram extracted along the mean displacement thickness (left) and the corresponding Fourier spectra (right) for case *S*. (a) zero FST; (b) $Tu = 0.005\%$. The dashed and solid lines correspond to the mean separation and reattachment locations, respectively.

The dominant frequency increases slightly for the cases with FST. The increase in frequency must be attributed to the smaller bubble dimensions. Smaller bubbles shed at higher frequencies.

From experiments and numerical simulations (Klebanoff & Tidstrom[19], Klebanoff[20], Jacobs & Durbin[15]; Fasel[21]), it is known that FST can cause the formation of streamwise elongated streaks inside the boundary layer, the so-called Klebanoff modes (K-modes). The K-modes lead to a significant distortion in the form of the u-component in the spanwise direction. K-modes are fundamentally different from TS-waves. Characteristic features of the K-modes are their low frequency, growth rate, high amplitude and a spanwise spacing of a few boundary layer thicknesses.

To determine the spanwise wavelength associated with the K-modes, one-dimensional power spectra of the streamwise velocity component are computed for case L and case S. The spectra were computed using spaniwse Fourier transform and the following relationship

$$E_{uu}(x,y,m) = \overline{u^m(x,y,t)u^m(x,y,t)}\,, \tag{8}$$

where the overbar indicates a time average and u^m symbolizes the Fourier transformed u-velocity component in spanwise direction with m as the spanwise modenumber (e.g. $m = 1$ indicates that the spanwise spacing of the modes is $\lambda_z = L_z$ and for $m = 2$, $\lambda_z = L_z/2$, and so on). Figure 8 shows the contours of spanwise, one-dimensional power spectra for selected streamwise locations: The inflow boundary, x_0, the onset of the adverse pressure gradient, x_{APG}, and the separation location, x_S. The wall-normal coordinate is normalized by the local boundary-layer thickness and the local displacement thickness is indicated by dashed lines in each plot.

For both cases with FST, the energy in the power spectrum at the inflow is clearly concentrated in the free-stream and the maximum amplitude is at $1 \leq m \leq 2$ (this is related to the chosen turbulent integral length scale L_{11}). While propagating in the downstream direction, the vortical structures in the free-stream enter the boundary layer as can be clearly observed at x_{APG}. At the onset of the adverse pressure gradient, the spanwise mode number with the largest disturbances amplitude is $m = 8$ for case L and $m = 6$ for case S. The disturbances are amplified further in the downstream direction.

Furthermore, the spanwise spacing of the Klebanoff modes based on the local boundary-layer thickness is in the order of $\lambda_{z,K} \approx (2.2\delta - 3\delta)$ for case L and $\lambda_{z,K} \approx (2.1\delta - 2.8\delta)$ for $5 \leq x \leq x_s$ where δ is the local boundary layer thickness and x_s is the separation location. These findings are consistent with the findings of $\lambda_{z,K} = O(2\delta - 4\delta)$ for attached flat-plate boundary layers (Kendall[22, 23], Westin *et al.*[24]).

The time- and spanwise-averages of the skin friction coefficient are compared in Fig. 69 for case L and case S for zero FST and $Tu = 0.005\%$. With the inclusion of FST, the separation location is slightly delayed and the reattachment location moves upstream for both cases, hence leading to shorter bubbles in the presence of FST. However, the reduction in the mean separation length is different for case L and case S: 17.5% for case L and 6.2% for case S.

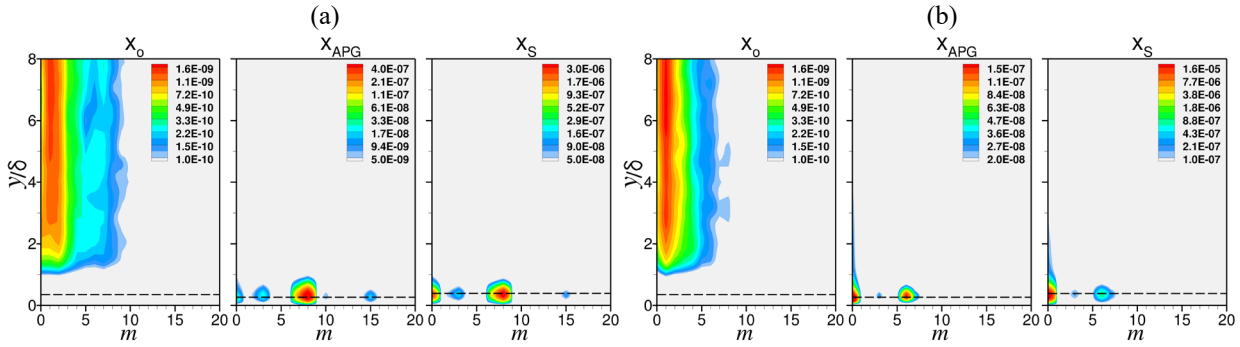

Figure 8. Spanwise one-dimensional energy spectra of the streamwise velocity at selected streamwise stations for $Tu = 0.005\%$ for case L (a) and case S (b). Dashed lines are the displacement thickness. Wall-normal coordinates was normalized with the local boundary layer thickness.

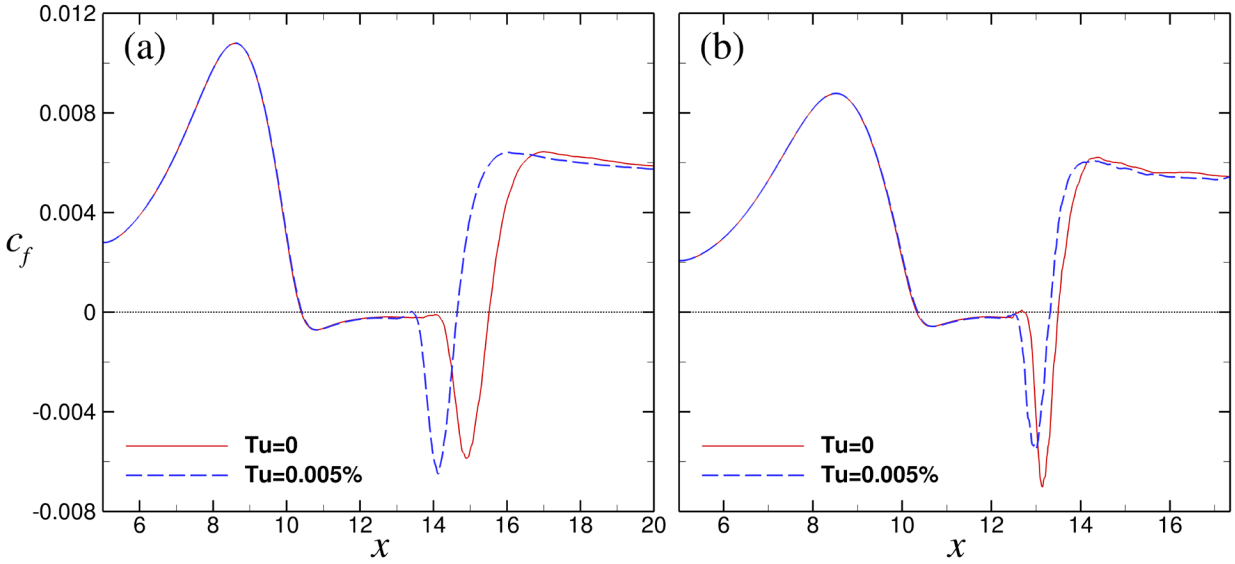

Figure 9. Time- and spanwise-averaged results for skin friction coefficient for case *L* (a) and case *S* (b).

V. Controlled Flow

In this section, simulations are discussed where high-amplitude 2D disturbance waves were introduced upstream of the separation location for cases *L* and *S* in the absence and presence of FST.

A. Hydrodynamic Instability

To determine the forcing frequency, the hydrodynamic instability w.r.t. two-dimensional unsteady disturbances is investigated. To predict the evolution of instabilities in the linear regime, we developed a numerical method to directly solve the Linearized Navier-Stokes Equations (LNSE) without relying on additional assumptions such as required by Linear Stability Theory (LST), i.e. assuming that the basic flow is parallel. Thus, all effects due to locally non-parallel effects of the basic flow are included in the LNSE approach.

The LNSE can be derived from the governing equations given in section III(A). The total flow field, $\boldsymbol{u}(\boldsymbol{x},t)$ & $\boldsymbol{\omega}(\boldsymbol{x},t)$, is decomposed into the base (or basic) flow $\boldsymbol{u_B}(x,y)$ & $\boldsymbol{\omega_B}(x,y)$ and small disturbances $\boldsymbol{u'}(\boldsymbol{x},t)$ & $\boldsymbol{\omega'}(\boldsymbol{x},t)$. When this disturbance ansatz is introduced into the Navier-Stokes equations (Eq. 1) the governing equations in disturbance form are obtained. The equations are then linearized (neglecting products of the disturbance quantities) and the governing equations for the base flow are subtracted in order to obtain the LNSE. For numerically solving the LNSE, the same time integration and spatial discretization techniques are employed as for the non-linear equations used in the DNS.

For the base flow in the LNSE investigations, the time- and spanwise-averaged results obtained for different uncontrolled flow conditions are employed. For the present linear instability investigations, 2D periodic disturbances of various frequencies were introduced at $x = 9.5$ by specifying a wall-normal velocity component. Then the amplitude development of the disturbances was tracked in downstream direction in order to extract the linear stability behavior. The results of such LNSE investigations are shown in Figs. 10 and 11 for case *L* and case *S*, respectively. The contours of wall-normal maxima of u-velocity disturbances are plotted in the frequency versus x for zero FST and $Tu = 0.005\%$. As can be observed in Figs. 10 and 11, the band width of amplified frequencies increases for case *S* compared to case *L*. From these plots, it is also obvious that there is a dominant frequency for all cases for which the disturbances reach the absolute maximum amplitudes:

- case *L*: $f^* = 256\ (hz)$ for $Tu = 0$ and $f^* = 264\ (hz)$ for $Tu = 0.005\%$.
- case *S*: $f^* = 740\ (hz)$ for $Tu = 0$ and $f^* = 760\ (hz)$ for $Tu = 0.005\%$.

Note that the dominant frequencies for case *S* are about 3 times higher than for case *L*, which can be cxplained by the fact the Reynolds number is higher for case *S*. Also, this is consistent with the results from DNS presented in the previous section.

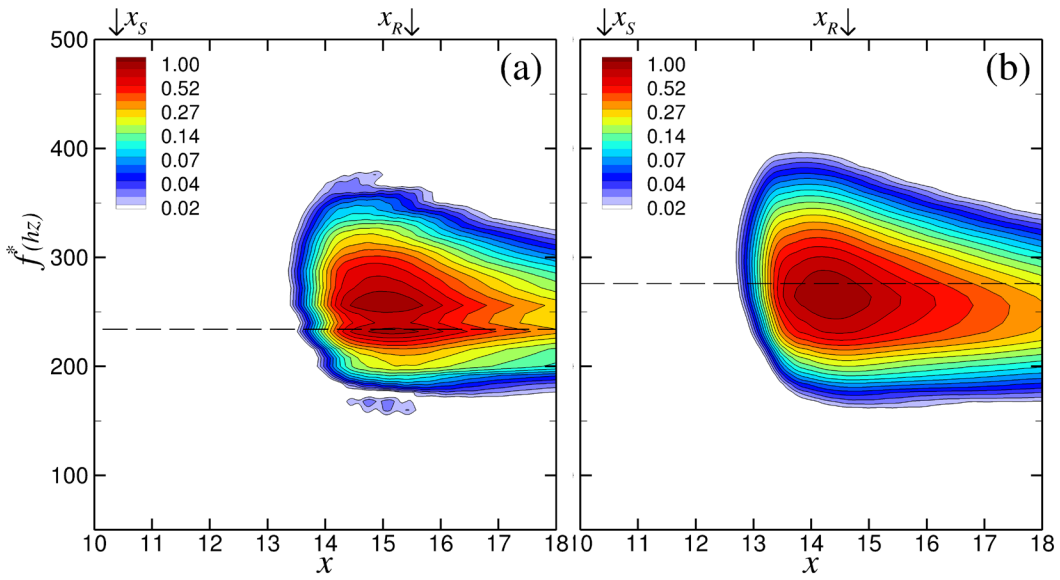

Figure 10. Contours of the wall-normal maximum amplitude of u-velocity in the frequency–x plane for case *L*. (a) zero FST; (b) $Tu = 0.005\%$. The dashed lines correspond to the shedding frequency obtained from the DNS. The mean separation and reattachment locations are marked by down arrows.

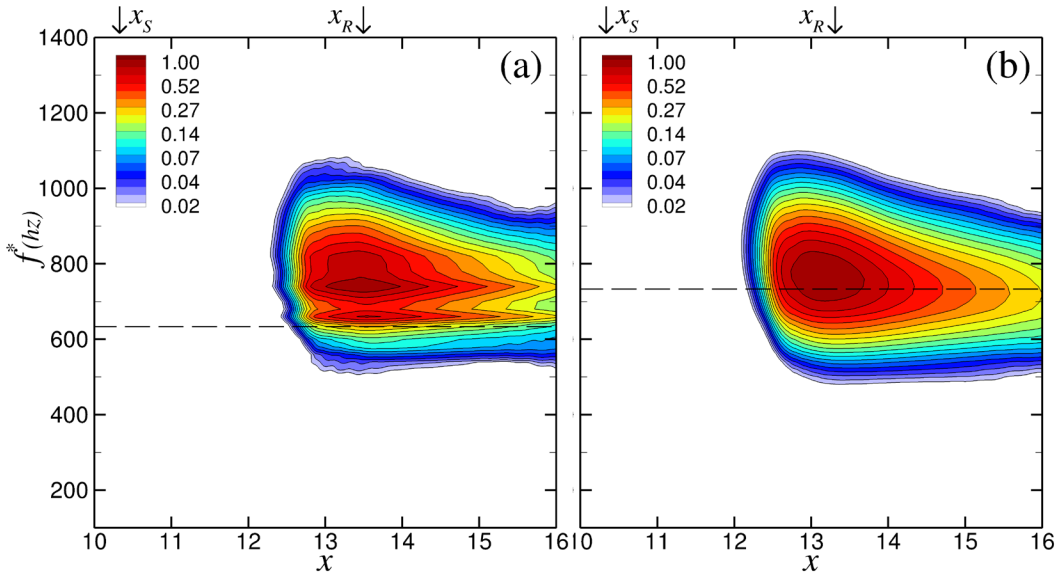

Figure 11. Contours of the wall-normal maximum amplitude of u-velocity in the frequency-x plane for case *S*. (a) zero FST; (b) $Tu = 0.005\%$. The dashed lines correspond to the shedding frequency obtained from the DNS. The mean separation and reattachment locations are marked by down arrows.

B. Instantaneous Flow Structures

In this section, the response of the flow to the 2D harmonic forcing for two different FST levels are discussed: Zero FST and very low FST ($Tu = 0.005\%$). The frequency of the actuation is the same for the zero FST and the $Tu = 0.005\%$ case and it is set to $f^* = 240\ (hz)$ for case L and $f^* = 667\ (hz)$ for case S based on the hydrodynamic instability analysis discussed above. Three different wall-normal forcing amplitudes are investigated: $A = 0.01$, $A = 0.03$ and $A = 0.05$. The width of the forcing slot was 0.2 and 0.13 for case L and case S, respectively. The forcing slot is located at the beginning of the adverse-pressure gradient region at $x_f = 9.5$.

The effect of the forcing on the LSB is demonstrated in Figs. 12 and 13 which show instantaneous contours of the spanwise vorticity for case L and case S, respectively. The visualizations for the zero FST cases reveal that the flow is "locking on" to the forcing signal and is shedding spanwise vortices at the forcing frequency. As discussed for the

results of the uncontrolled flow, these structures are very effective in increasing the wall-normal momentum transfer and therefore reducing the size of the separation bubble. The vortices remain close to the wall and transition to turbulence is delayed significantly. For case L, transition does not occur inside the integration domain for the two lowest forcing amplitudes ($A = 0.01$ and $A = 0.03$). In fact, the flow remains completely laminar in the entire integration domain. This result is in agreement with the findings of Embacher & Fasel.[2] When the forcing amplitude is increased, small scale fluctuations become visible in the downstream part of the domain.

For case S which corresponds to the higher Reynolds number, the vortex shedding still "locks on" to the forcing frequency and a train of 2D spanwise rollers is observed for different forcing amplitudes. Compared to the case L, the transition process starts further upstream. For $A = 0.01$, the spanwise structures are seen to break up into smaller scales for $x > 17$ which indicates the onset of transition.

In the presence of FST environment, the situation changes. Figures 12(b) and 13(b) reveal that with FST the strong spanwise structures break-up into smaller scales soon after their first appearance such that transition to turbulence is initiated. In fact, prior to transition only one or two spanwise coherent structures are still visible depending on the forcing amplitude. It must therefore be assumed, that the relaminarization of the flow for the zero FST cases is indeed an artifact of the extremely low "noise" level of the highly-accurate DNS code, which does not occur in a realistic environment even with very low FST conditions.

To gain more insight into the response of the boundary layer to the 2D forcing and the transition process, the λ_2-criterion by Jeong & Hussain[25] is employed. The λ_2-criterion indicates areas where rotation dominates strain. Figures 14 and 15 provides instantaneous perspective views of iso-surfaces of the λ_2-criterion colored by the streamwise velocity for case L and case S. Also shown are instantaneous, spanwise-averaged ω_z-vorticity contours. The visualizations show the train of spanwise "rollers" in the absence of FST.

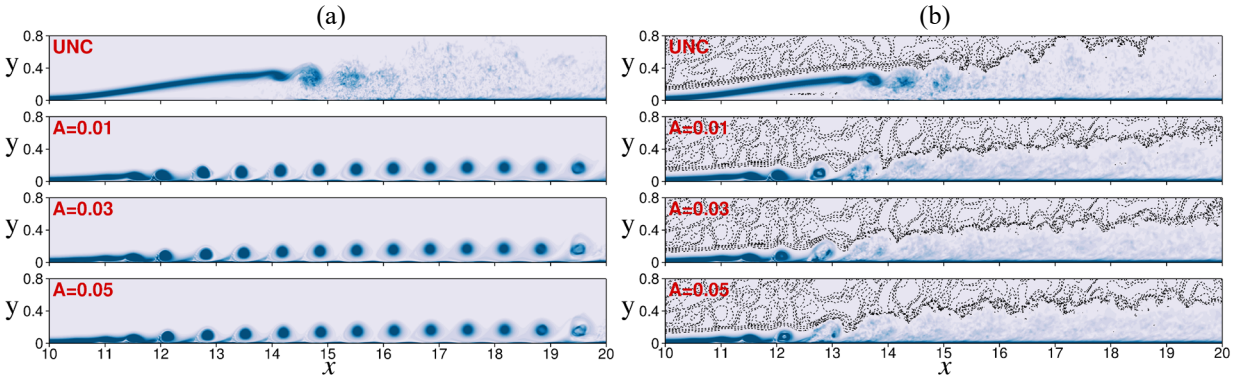

Figure 12. Instantaneous contours of spanwise vorticity (average in spanwise direction) for various forcing amplitudes for case *L*. (a) zero FST; (b) $Tu = 0.005\%$. The case "UNC" corresponds to the uncontrolled flow.

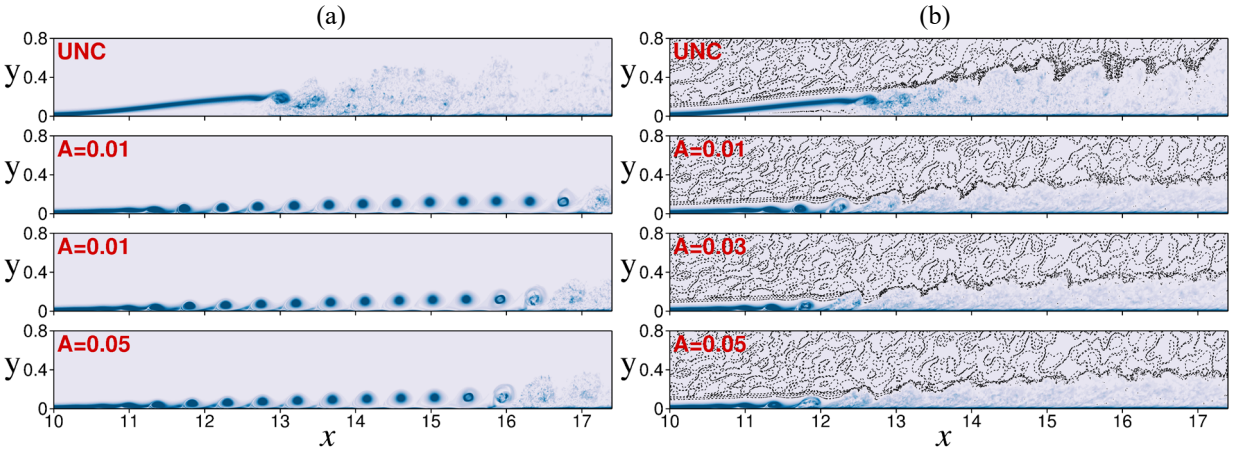

Figure 13. Instantaneous contours of spanwise vorticity (average in spanwise direction) for various forcing amplitudes for case *S*. (a) zero FST; (b) $Tu = 0.005\%$. The case "UNC" corresponds to the uncontrolled flow.

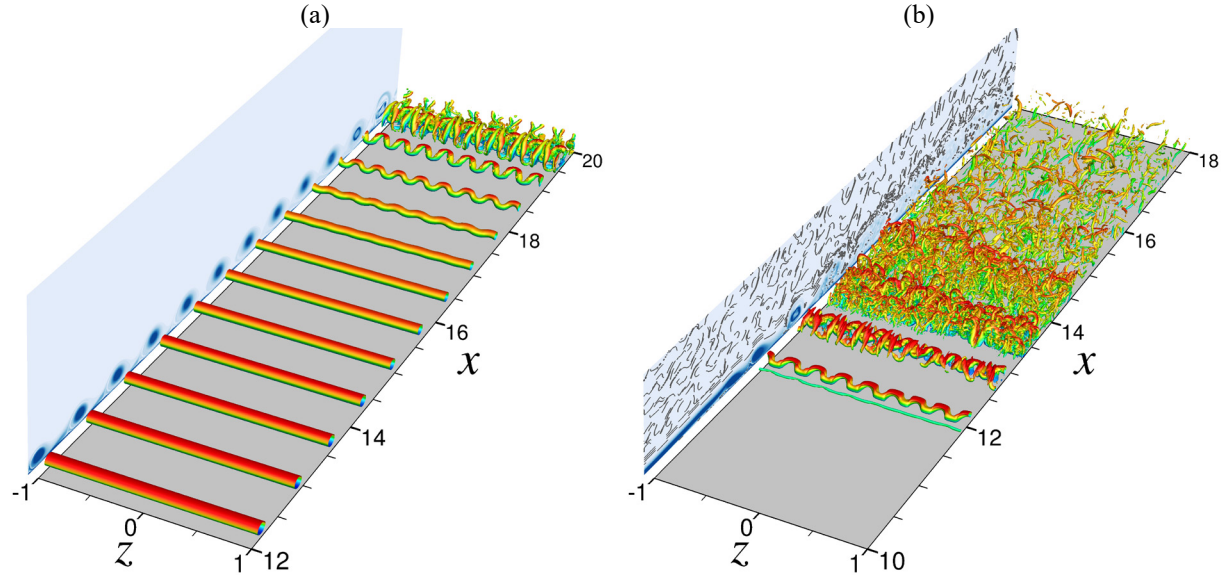

Figure 14. Instantaneous flow visualization for case *L*. Shown are $\lambda_2 = -40$ colored by u-velocity together with contours of ω_z-vorticity (averaged in spaniwse direction). (a) zero FST, A=0.05; (b) Tu=0.005%, A=0.01.

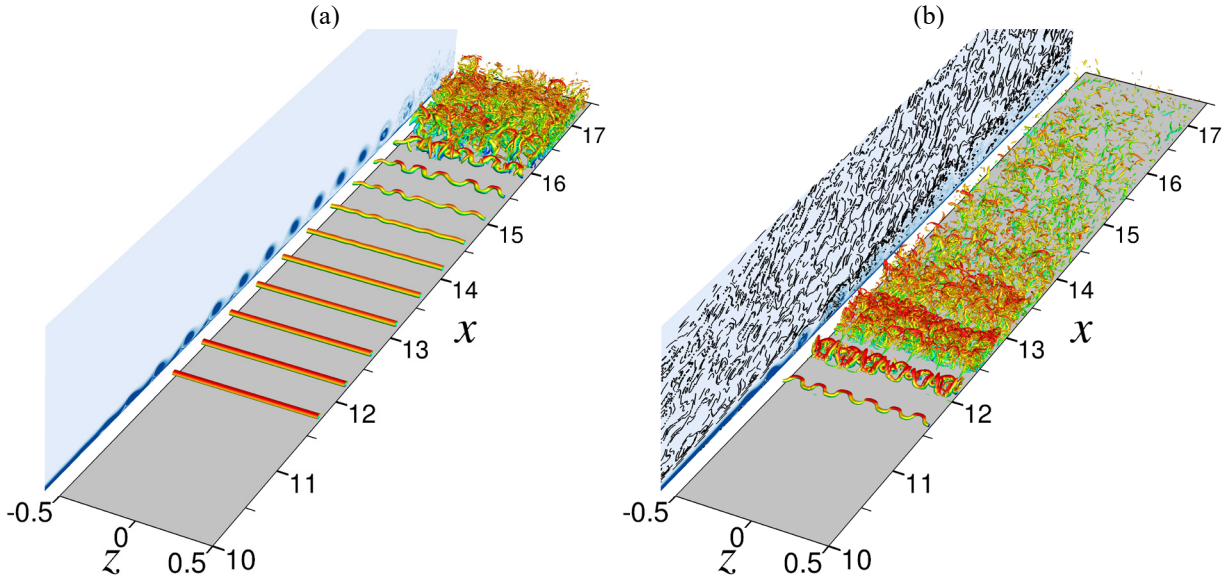

Figure 15. Instantaneous flow visualization for case *S*. Shown are $\lambda_2 = -150$ colored by u-velocity together with contours of ω_z-vorticity (averaged in spaniwse direction). (a) zero FST, A=0.05; (b) Tu=0.005%, A=0.01.

Without FST, transition to turbulence is delayed until further downstream, where the primary vortex cores appear to be deformed sinusoidally in the spanwise direction due to the secondary instability of the periodic controlled baseflow. For a forcing amplitude of $A = 0.05$, the spanwise wavelength of the amplified 3D disturbance waves is $\lambda_z = 0.25$ for case L and $\lambda_z = 0.2$ for case S, which are in the order of the shear-layer thickness for both cases. It is worth noting that the ratio of the spanwise wavelength to the streamwise wavelength of the disturbance waves in the transition region is $\lambda_z/\lambda_x \approx 0.37$ and $\lambda_z/\lambda_x \approx 0.44$ for case L and case S, respectively.

A secondary stability analysis by von Terzi[26] revealed that the most unstable spanwise wavelengths were in the range $0.3 \leq \lambda_z/\lambda_x \leq 0.6$ for the separated shear-layer developing behind a backward-facing step. Our previous study (Hosseinverdi & Fasel[27]) showed that the development of streamwise vortices in the 'braid' region (region which connects the bottom of one vortex core with the top of an adjoining vortex structure), between two neighboring spanwise vortices, may be associated with the instability that is comparable to that of an elliptic instability as observed in bluff-body wakes.

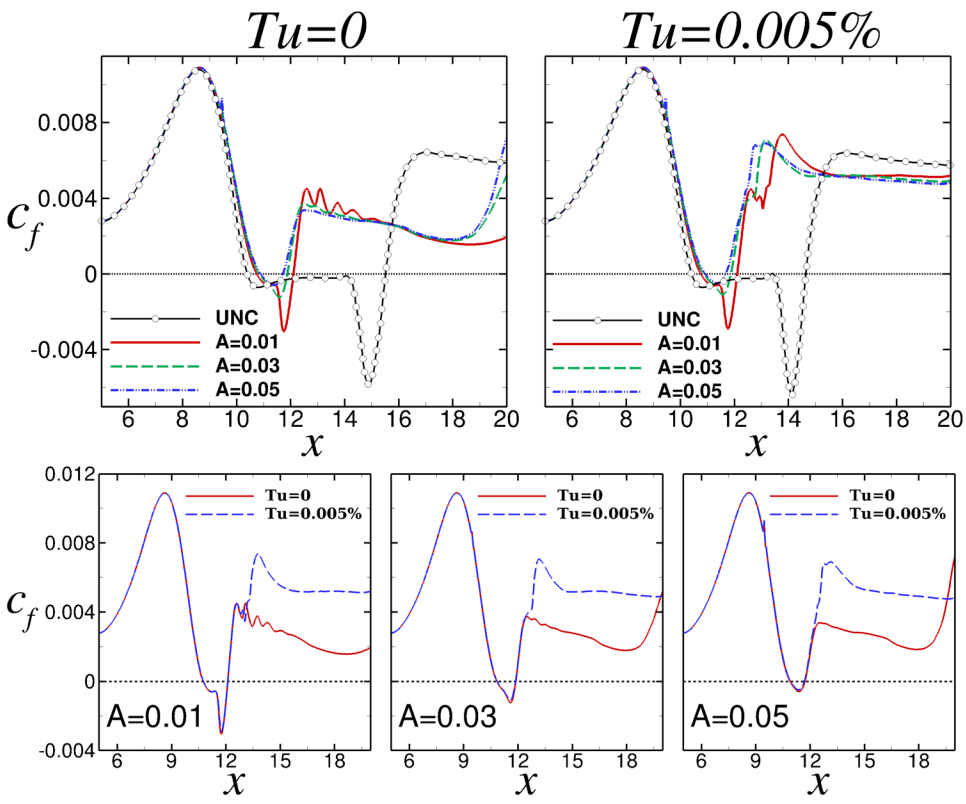

Figure 16. Comparison of skin friction coefficients for case *L*.

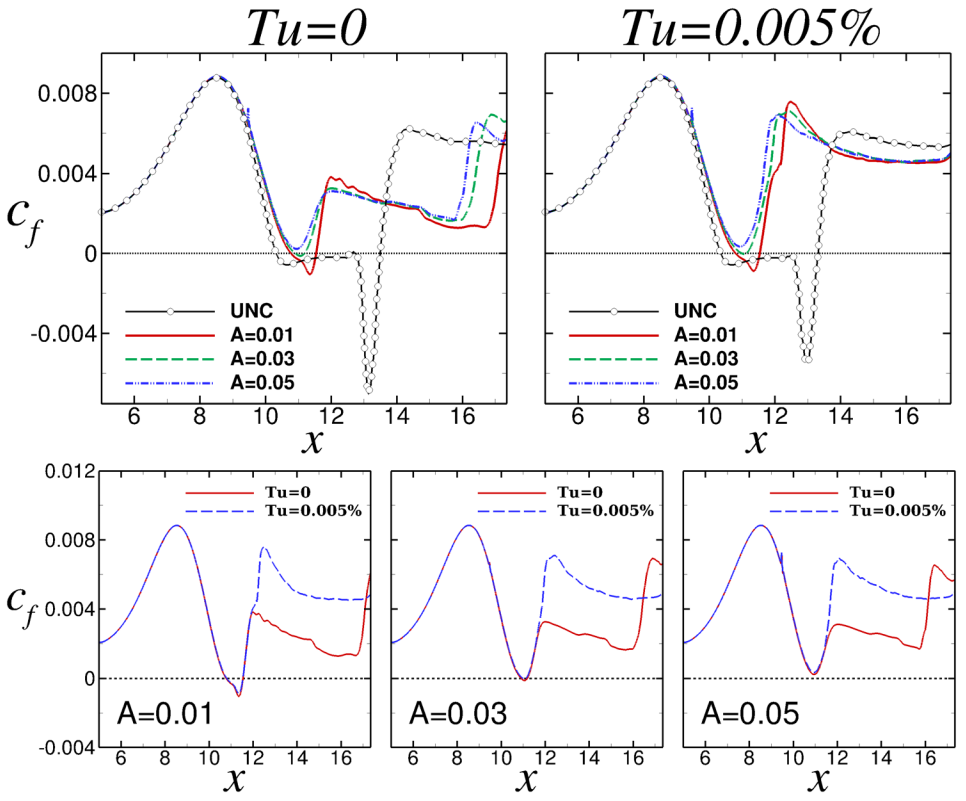

Figure 17. Comparison of the skin friction coefficients for case *S*.

For the cases with FST, 3D disturbances do assume finite amplitudes. As a result, the primary vortex cores appear modulated in the spanwise direction shortly after the reattachment location. The spanwise spacing agrees very well with the spanwise spacing of the Klebanoff modes (see Fig. 8). Therefore, these results hint at a strong interaction between the spanwise modulation due to the Klebanoff modes and the 2D spanwise vortices, which ultimately causes transition of the flow.

A comparison of the time- and spanwise-averaged skin-friction coefficients for the uncontrolled and the controlled flows is presented in Figs. 16 and 17 for case L and case S, respectively. In each figure, the top-left graph is for $Tu = 0$ and the top-right graph is for $Tu = 0.005\%$. Comparisons of the c_f for the zero FST case and the FST case are presented in the bottom plots.

For a given forcing amplitude, the forcing of strong 2D waves leads to virtually identical bubble sizes independent of the FST. This leads to the conclusion that the stunning effectiveness of the flow control is a consequence of the wall-normal momentum exchange caused by the strong 2D "rollers", rather than the accelerated transition in the cases with FST.

C. Disturbance Evolution: The Interaction Between Klebanoff-Modes and the 2D Primary Waves

The flow visualizations in Figs. 14 and 15 suggest that a strong interaction between the spanwise modulations caused by FST and the primary spanwise vortices exists since the spanwise wavelength of the vortex distortions is identical to the spacing of the Klebanoff modes.

By tracking the downstream development of the disturbance waves, information can be gained regarding the nature of the instability mechanisms. Toward this end, the flow data were Fourier decomposed in the spanwise direction as well as in time. The notation (h, m) is used for a pair of mode numbers. Here, h/T is the frequency and $2\pi m/L_z$ is the spanwise wavenumber of a disturbance wave. Furthermore, T is the period of the actuation and L_z is the spanwise domain width. Hence, (0, 0) represents the time- and spanwise-averaged flow and (1, 2) denotes a harmonic wave of period T with $\lambda_z = L_z/2$ and so on. For the Fourier transform in time, time-dependent DNS data were sampled over 40 forcing periods, T, with 30 samples per period.

The disturbance amplitude for each mode (h, m) was computed from the wall-normal integration of the Fourier amplitude of disturbance u-velocity component inside the boundary-layer,

$$A_u^{(h,m)}(x) = \sqrt{\frac{1}{\delta(x)} \int_0^{\delta(x)} u_A^{(h,m)}(x,y)^2 \, dy} \,, \tag{9}$$

where $\delta(x)$ is the local boundary-layer thickness. The downstream evolution of the Fourier amplitudes for the steady and unsteady disturbance waves for case S for zero FST and $Tu = 0.005\%$ are provided in Fig. 18, but only the modes that reach high non-linear amplitudes are highlighted.

For a forcing amplitude of $A = 0.03$ and in the absence of FST, the 2D disturbance wave at the fundamental frequency, (1,0), experience exponential growth and grows several orders of magnitude until non-linear saturation. In addition, it remains at much larger amplitude levels compared to the 3D disturbances. For $x > 14$ the 2D mode amplitude decays. This behavior can be correlated with the onset of the spanwise modulation of the primary vortices (see Fig. 15a).

In addition to the strong amplification of 2D modes, the steady and unsteady 3D disturbance modes grow from very small amplitudes in the order of 10^{-13} (numerical round-off). In particular, the unsteady mode (1,6) increases suddenly by approximately one order of magnitude at the forcing location. The unsteady disturbance mode (1,6) exhibits much higher amplification rates than that of the 2D wave, which could be an indication of a secondary instability mechanism. The strong amplification can also be observed for the 3D steady disturbance mode (0,6). Despite the large secondary amplification rates, modes (0,6) and (1,6) need a long downstream extent before they reach the amplitude level of the 2D wave, and transition is initiated when this occurs (at $x = 15.6$).

The same characteristics are observed for $A = 0.05$. However, disturbances with spanwise modenumber $m = 5$ also play an important role in the transition process in addition to the disturbances with $m = 6$.

The spanwise modenumber associated with the Klebanoff mode is $m = 6$. Thus, with low level FST, the transition process is governed by the interaction of the 2D wave with the forcing frequency and the steady and unsteady disturbance modes with the spanwise modenumber $m = 6$ as shown in Fig. 18 (bottom plots). At the forcing location, $x_f = 9.5$, the amplitude of the unsteady 3D mode (1,6) increases suddenly by approximately one order of magnitude. This sudden increase can be explained by the non-linear interaction of the (1,0) fundamental disturbance mode and the (0,6) disturbance (Klebanoff) modes.

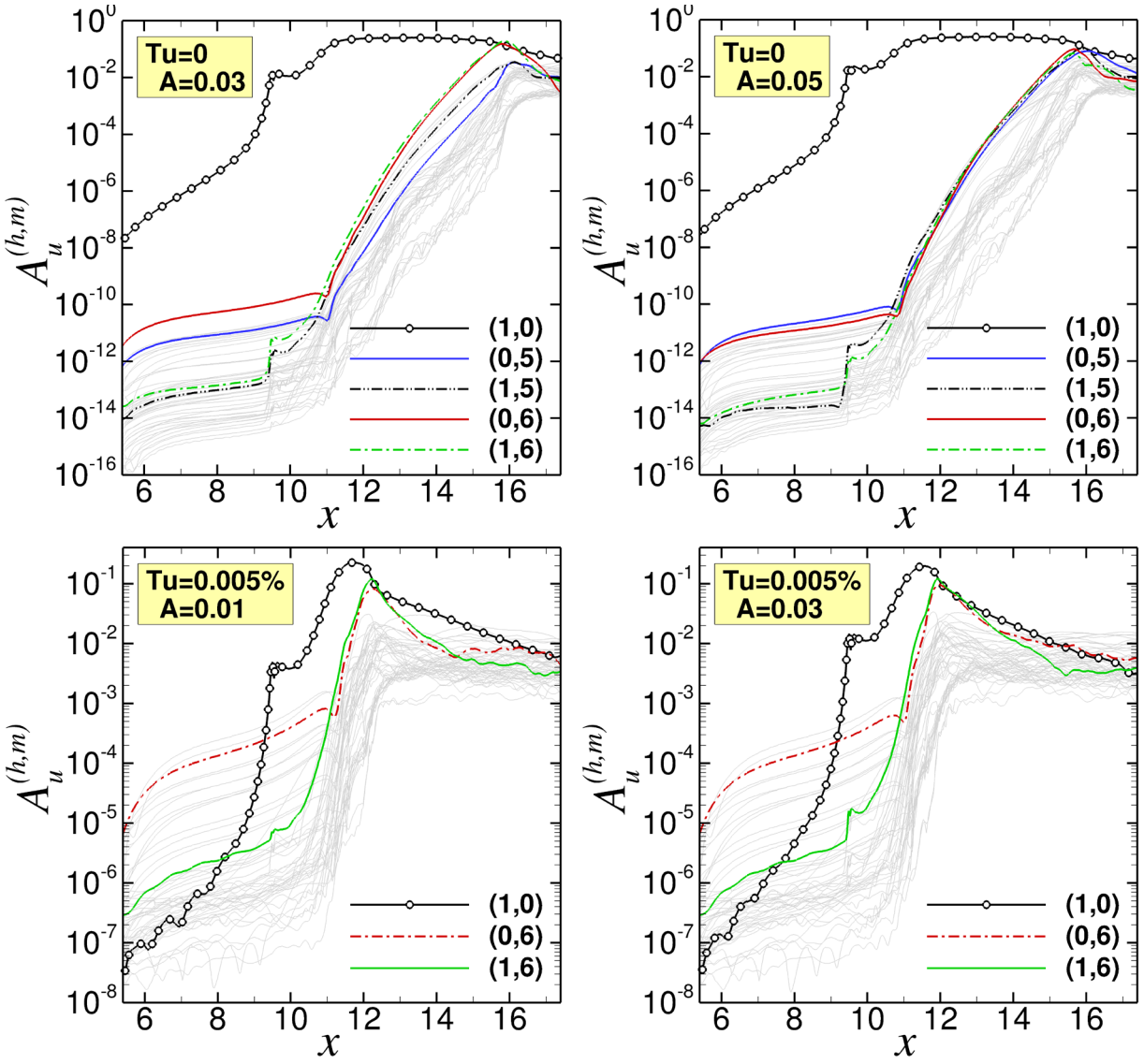

Figure 18. Downstream development of the Fourier amplitudes for steady and unsteady modes of case *S*.

VI. Summary and Conclusion

High-resolution direct numerical simulations of canonical separation bubbles on a flat plate were carried out and the response to high-amplitude 2D forcing was investigated in the absence of and in the presence of free-stream turbulence. Harmonic blowing and suction through a spaniwse slot was shown to be very effective in eliminating laminar separation. This was attributed to the shear-layer instability, which amplifies the disturbance input. Without FST, the controlled flow is virtually two-dimensional and dominated by strong spanwise vortices. This suggests that the control is effective in suppressing temporally-growing disturbances.

Isotropic turbulence velocity fluctuations, which are generated based on a superposition of the continuous modes of the Orr-Sommerfeld and Squire equations, were seeded at the inflow boundary of the computational domain. In the presence of FST the shear-layer instability was also found to amplify the controlled disturbance input which makes the flow control equally efficient as for the zero FST case. However, with FST the transition delay and relaminarization could no longer be accomplished. This is an important finding as “clean” simulations where the FST is neglected (zero FST) appear to be not realistic when separation control and transition are investigated. In the presence of even very low FST level, the flow transitions shortly after reattachment location even when purely 2D disturbances are introduced upstream. This can be explained by the fact that in the presence of even very small levels FST, strong interactions occur between the high-amplitude 2D disturbance waves introduced by the forcing and the 3D Klebanoff modes that are excited by the FST.

Acknowledgments

This work was supported by the Air Force Office of Scientific Research (AFOSR) under grant number FA9550-14-1-0184, with Dr. Douglas R. Smith serving as the program manager.

References

[1]Gaster, M., "The structure and behaviour of laminar separation bubbles," *AGARD CP 4*, pp. 813–854, 1996.

[2]Embacher, M. and Fasel, H. F., "Direct numerical simulations of laminar separation bubbles: investigation of absolute instability and active flow control of transition to turbulence," *J. Fluid Mech*, Vol. 747, 2014, pp. 141–185.

[3]Benton, S.I and Visbal, M.R., "Investigation of High-Frequency Separation Control Mechanisms for Delay of Unsteady Separation," AIAA 2016-4241.

[4]Jones, L.E., Sandberg, R.D and Sandham, N.D., "Direct numerical simulations of forced and unforced separation bubbles on an airfoil at incidence," *J. Fluid. Mech*, Vol. 602, 175-207, 2008.

[5]Balzer, W and Fasel, H.F., "Direct Numerical Simulation of Laminar Boundary-Layer Separation and Separation Control on the Suction Side of an Airfoil at Low Reynolds Number Conditions," *AIAA Paper*, AIAA-2010-4866.

[6]Visbal, M. R., "Control of Dynamic Stall on a Pitching Airfoil Using High-Frequency Actuation," *AIAA Paper*, No. AIAA 2015-1267, 2015.

[7]Owen, P. R. & Klanfer, L., "On the laminar boundary layer separation from the leading edge of a thin airfoil," In ARC CP 220, 1953.

[8]Diwan, S. S., Chetan, S. J and Ramesh, O. N., "On the bursting criterion for laminar separation bubbles," In *Laminar-Turbulent Transition, Proceedings of the IUTAM Symposium*, pp. 401–407. Bangalore, India, 2006.

[9]Meitz, H. & Fasel, H. F., 'A compact-difference scheme for the Navier-Stokes equations in vorticity-velocity formulation,' *J. Comp. Phys*. 157, 371–403, 2000.

[10]Balzer, W. & Fasel, H. F., 'Numerical investigation of the effect of free-stream turbulence on laminar boundary-layer separation.' *AIAA Paper*, AIAA-2010-4600, 2010.

[11]Hosseinverdi, S., Balzer, W., and Fasel, H., "Direct Numerical Simulations of the Effect of Free-Stream Turbulence on 'Long' Laminar Separation Bubbles," *AIAA Paper,* AIAA-2012-2972, 2012.

[12]Hosseinverdi, S., and Fasel, H.F., "Direct Numerical Simulations of Laminar-to-Turbulent Transition in Laminar Separation Bubbles in Three-Dimensional Boundary-Layer," *AIAA Paper*, AIAA-2016-1965, 2016.

[13]Hosseinverdi, S., and Fasel, H.F., "Numerical Investigations of the Effect of Free-Stream Turbulence on Separation Control by Pulsed Vortex Generator Jets," *AIAA Paper*, AIAA-2013-2614, 2013.

[14]Postl, D., Balzer, W., and Fasel, H. F., "Control of laminar separation using pulsed vortex generator jets: direct numerical simulations," *J. Fluid Mechanics*. 676, 81-109, 2011.

[15]Jacobs, R. G & Durbin, P.A., 'Simulations of Bypass Transition,' *J. Fluid Mech*, vol. 421, 185-212, 2001.

[16] Brandt, L., Schlatter, P. & Henningson, D. S., "Transition in boundary layers subject to free-stream turbulence," *J. Fluid Mech*. 517, 167–198, 2004.

[17]Grosch, C. E. and Salwen, H., "The continuous spectrum of the Orr-Sommerfeld equation. Part 1. The spectrum and the eigenfunctions," *J. Fluid Mech.*, Vol. 68, pp. 33–54, 1978.

[18]Liu, Y., Zaki, T. A., and Durbin, P. A., "Boundary-layer transition by interaction of discrete and continuous modes," *J. Fluid Mech*, vol. 604, 199-233, 2008.

[19]Klebanoff, P. S. and Tidstrom, K. D., "Evolution of amplified waves leading to transition in a boundary layer with zero pressure gradient," *NASA TN D 195*, 1959.

[20]Klebanoff, P., "Effect of freestream turbulence on the laminar boundary layer," *Bull. Am. Phys. Soc*, v. 10, 1971.

[21]Fasel, H. F. 'Numerical investigation of the interaction of the Klebanoff-mode with a Tollmien-Schlichting wave.' *J. Fluid Mech*. 450, 1–33, 2002.

[22]Kendall, J. M., "Experimental study of disturbances produced in a pretransitional laminar boundary layer by weak freestream turbulence," *AIAA Paper 1985-1695*, 1985.

[23]Kendall, J. M., "Boundary layer receptivity to freestream turbulence," *AIAA Paper*, AIAA-1990-1504, 1990.

[24]Westin, K. J. A., Boiko, A. V., Klingmann, B., B. G., Kozlov, V., V. and Alfredsson, P. H., "Experiments in a boundary layer subjected to freestream turbulence. part 1. boundary layer structure and receptivity." *J. Fluid Mech*. 281, 193–218, 1994.

[25]Jeong, J. & Hussain, F., "On the identification of a vortex," *J. Fluid Mech*. 285, 69–94, 1995.

[26]von Terzi., "Numerical investigation of transitional and turbulent backward-facing step flows," *PhD thesis*, University of Arizona.

[27]Hosseinverdi, S., and Fasel, H.F., "Direct Numerical Simulations of Transition to Turbulence in Two-Dimensional Laminar Separation Bubbles," *AIAA Paper*, AIAA-2013-0264, 2013.